Journal of Physics: Condensed Matter

PAPER • **OPEN ACCESS**

Ultrafast optical currents in gapped graphene

To cite this article: S Azar Oliaei Motlagh *et al* 2020 *J. Phys.: Condens. Matter* **32** 065305

View the article online for updates and enhancements.

IOP ebooks™

Bringing you innovative digital publishing with leading voices to create your essential collection of books in STEM research.

Start exploring the collection - download the first chapter of every title for free.

This content was downloaded from IP address 170.140.163.185 on 07/11/2019 at 02:42

OPEN ACCESS
IOP Publishing
Journal of Physics: Condensed Matter
J. Phys.: Condens. Matter **32** (2020) 065305 (8pp)
https://doi.org/10.1088/1361-648X/ab4fc7

Ultrafast optical currents in gapped graphene

S Azar Oliaei Motlagh, Fatemeh Nematollahi, Aranyo Mitra, Ahmal Jawad Zafar, Vadym Apalkov and Mark I Stockman

Center for Nano-Optics (CeNO) and Department of Physics and Astronomy, Georgia State University, Atlanta, GA 30303, United States of America

E-mail: azar.oliaei@gmail.com

Received 20 August 2019, revised 5 October 2019
Accepted for publication 21 October 2019
Published 4 November 2019

Abstract

We theoretically study the interaction of ultrashort optical pulses with gapped graphene. Such a strong pulse results in a finite conduction band population and a corresponding electric current, both during and after the pulse. Since gapped graphene has broken inversion symmetry, it has an axial symmetry about the y-axis but not about the x-axis. We show that, in this case, if the linear pulse is polarized along the x-axis, the rectified electric current is generated in the y direction. At the same time, the conduction band population distribution in the reciprocal space is symmetric about the x-axis. Thus, the rectified current in gapped graphene has an inter-band origin, while the intra-band contribution to the rectified current is zero.

Keywords: graphene, gapped graphene, current, ultrafast electron dynamics, ultrafast laser pulse, topological resonances, transferred charge

(Some figures may appear in colour only in the online journal)

1. Introduction

The availability of ultrashort laser pulses with the duration of a few femtoseconds provides effective tools to manipulate and study the electron dynamics in solids at ultrafast time scale with high temporal resolution [1–20]. Among solids, two dimensional (2D) crystalline materials exhibit unique properties due to the confinement of electron dynamics to a plane [21]. Graphene, a layer of carbon atoms with the thickness of one atom, is a well known 2D material with fascinating properties. Graphene has a honeycomb crystal structure made of two sublattices, A and B—see figure 1(a) [22, 23]. Having two Dirac points, K' and K at the edges of the Brillouin zone -see figure 1(b), makes graphene a suitable platform to study the dynamics of massless Dirac fermions [21–24]. In graphene, both time reversal and inversion symmetries are conserved. However, there is a broad class of semiconductors with honeycomb crystal structure where two sublattices are made of two different atoms, and the inversion symmetry is broken, which results in a finite band gap at the K and K' points [25, 26]. One of such materials is a monolayer of transition metal dichalcogenides (TMDCs) that has a direct band gap with nonzero Berry curvature around the K' and K valleys. Gapped graphene, which has broken inversion symmetry, has topological properties similar to TMDC monolayer. Namely, the Berry curvature in gapped graphene is extended over the finite region near the K and K' points. Such broadening of the Berry curvature, which can be tuned by the band gap, results in nontrivial topological properties of gapped graphene [19, 25, 27, 28]. One of such properties is a recently predicted topological resonance, which produces finite valley polarization in TMDCs and gapped graphene [18, 29].

In this article, we study the ultrafast nonlinear electron dynamics in gapped graphene. The dynamics is induced by a single cycle ultrafast linearly polarized pulse. Although, the linear pulse does not produce any residual valley polarization; it results in electric current, the magnitude and the direction of which can be controlled by the band gap. Gapped graphene, considered in the present article, is a model of direct band gap semiconductors with honeycomb lattice structures. Opening of the band gap in graphene can be achieved by several

Original content from this work may be used under the terms of the Creative Commons Attribution 3.0 licence. Any further distribution of this work must maintain attribution to the author(s) and the title of the work, journal citation and DOI.

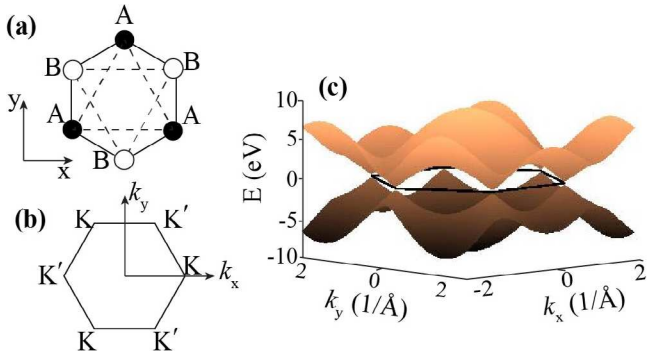

Figure 1. (a) The honeycomb lattice structure of graphene is made of two triangular sublattices A (black circle) and B (white circle). (b) The first Brillouin zone of the honeycomb lattice has two valleys K and K' located in its boundaries. (c) The energy dispersion is shown for gapped graphene with a band gap of 0.5 eV in the extended zone. The solid black lines show the boundaries of the first Brillouin zone.

methods, for example, by placing graphene on boron nitride (BN) or silicon carbide (SiC) substrate [30, 31].

2. Model and main equations

In the presence of an applied ultrafast optical pulse, $\mathbf{F}(t)$, with the duration of less than 5 fs, the electron dynamics is coherent. This assumption is valid since the electron scattering time in 2D materials is longer than 10 fs [32–37]. To find the coherent electron dynamics in gapped graphene, we solve the time-dependent Schrödinger equation (TDSE)

$$\mathrm{i}\hbar\frac{\mathrm{d}\Psi}{\mathrm{d}t} = H(t)\Psi, \tag{1}$$

with the Hamiltonian

$$H(t) = H_0 - e\mathbf{F}(t)\mathbf{r}, \tag{2}$$

where e is an electron charge, and H_0 is the nearest neighbor tight binding Hamiltonian of gapped graphene [38],

$$H_0 = \begin{pmatrix} \frac{\Delta_g}{2} & \gamma f(\mathbf{k}) \\ \gamma f^*(\mathbf{k}) & -\frac{\Delta_g}{2} \end{pmatrix}. \tag{3}$$

Here Δ_g is the band gap, $\gamma = -3.03$ eV is the hopping integral, and

$$f(\mathbf{k}) = \exp\left(\mathrm{i}\frac{ak_y}{\sqrt{3}}\right) + 2\exp\left(-\mathrm{i}\frac{ak_y}{2\sqrt{3}}\right)\cos\left(\frac{ak_x}{2}\right), \tag{4}$$

where $a = 2.46$ Å is a lattice constant. The eigenenergies of the tight-binding Hamiltonian, H_0, can be found as follows

$$E_c(\mathbf{k}) = +\sqrt{\gamma^2\left|f(\mathbf{k})\right|^2 + \frac{\Delta_g^2}{4}}, \tag{5}$$

$$E_v(\mathbf{k}) = -\sqrt{\gamma^2\left|f(\mathbf{k})\right|^2 + \frac{\Delta_g^2}{4}}, \tag{6}$$

where c and v stand for the conduction band (CB) and the valence band (VB), respectively. Figure 1(c) shows the calculated energy dispersion from equations (5) and (6) for the band gap of $\Delta_g = 0.5$ eV.

The coherent electron dynamics in solids has two major components: intraband and interband dynamics. The intraband dynamics is governed by the Bloch acceleration theorem

$$\hbar\frac{\mathrm{d}\mathbf{k}}{\mathrm{d}t} = e\mathbf{F}(t). \tag{7}$$

The solution of this equation has the following form

$$\mathbf{k}(\mathbf{q}, t) = \mathbf{q} + \frac{e}{\hbar}\int_{-\infty}^{t}\mathbf{F}(t')\mathrm{d}t', \tag{8}$$

where $\mathbf{q}$ is the initial crystal wavevector of an electron in the first Brillouin zone.

The corresponding wave functions, which are the solutions of Schrödinger equation (1) within a single band α, i.e. without interband coupling, are the Houston functions [39],

$$\Phi^{(\mathrm{H})}_{\alpha\mathbf{q}}(\mathbf{r}, t) = \Psi^{(\alpha)}_{\mathbf{k}(\mathbf{q},\mathbf{t})}(\mathbf{r})\exp\left(\mathrm{i}\phi^{(\mathrm{d})}_{\alpha}(\mathbf{q}, t) + \mathrm{i}\phi^{(\mathrm{B})}_{\alpha}(\mathbf{q}, t)\right), \tag{9}$$

where $\alpha = v, c$ stand for the VB and CB, respectively, $\Psi^{(\alpha)}_{\mathbf{k}}$ are Bloch-band eigenstates in the absence of the external field, $E_\alpha(\mathbf{k})$ are the eigenenergies, and the dynamic phase, $\phi^{(\mathrm{D})}_{\alpha}$, and geometric phase, $\phi^{(\mathrm{B})}_{\alpha}$, are defined as

$$\phi^{(\mathrm{D})}_{\alpha}(\mathbf{q}, t) = \frac{-1}{\hbar}\int_{-\infty}^{t}\mathrm{d}t'\left(E_\alpha[\mathbf{k}(\mathbf{q}, t')]\right), \tag{10}$$

$$\phi^{(\mathrm{B})}_{\alpha}(\mathbf{q}, t) = \frac{e}{\hbar}\int_{-\infty}^{t}\mathrm{d}t'\mathbf{F}\left(\boldsymbol{\mathcal{A}}^{\alpha\alpha}[\mathbf{k}(\mathbf{q}, t')]\right). \tag{11}$$

Here $\boldsymbol{\mathcal{A}}^{\alpha\alpha} = \left\langle\Psi^{(\alpha)}_{\mathbf{q}}\middle|\mathrm{i}\frac{\partial}{\partial\mathbf{q}}\middle|\Psi^{(\alpha)}_{\mathbf{q}}\right\rangle$ is the intraband Berry connection. The expressions for the intraband Berry connections, $\boldsymbol{\mathcal{A}}^{\alpha\alpha} = (\mathcal{A}^{\alpha\alpha}_x, \mathcal{A}^{\alpha\alpha}_y)$, can be found from the tight-binding Hamiltonian as follows

$$\mathcal{A}^{\alpha\alpha}_x(\mathbf{k}) = \frac{-a\gamma^2}{\gamma^2|f(\mathbf{k})|^2 + (\Delta_g/2 - E_\alpha)^2}\sin\frac{3ak_y}{2\sqrt{3}}\sin\frac{ak_x}{2}, \tag{12}$$

$$\mathcal{A}^{\alpha\alpha}_y(\mathbf{k}) = \frac{a\gamma^2}{\sqrt{3}\left(\gamma^2|f(\mathbf{k})|^2 + (\Delta_g/2 - E_\alpha)^2\right)} \times\left(\cos ak_x - \cos\frac{\sqrt{3}ak_y}{2}\cos\frac{ak_x}{2}\right). \tag{13}$$

The interband electron dynamics is described by TDSE (1). The solution of TDSE can be expanded in the basis of Houston functions $\Phi^{(H)}_{\alpha\mathbf{q}}(\mathbf{r}, t)$ [39],

$$\Psi_{\mathbf{q}}(\mathbf{r}, t) = \sum_{\alpha=c,v}\beta_{\alpha\mathbf{q}}(t)\Phi^{(H)}_{\alpha\mathbf{q}}(\mathbf{r}, t), \tag{14}$$

where $\beta_{\alpha\mathbf{q}}(t)$ are expansion coefficients, which satisfies the following system of coupled differential equations

$$\mathrm{i}\hbar\frac{\partial B_{\mathbf{q}}(t)}{\partial t} = H'(\mathbf{q}, t)B_{\mathbf{q}}(t), \tag{15}$$

where the wave function (vector of state) $B_q(t)$ and Hamiltonian $H'(\mathbf{q}, t)$ are defined as

$$B_{\mathbf{q}}(t) = \begin{bmatrix} \beta_{c\mathbf{q}}(t) \\ \beta_{v\mathbf{q}}(t) \end{bmatrix}, \tag{16}$$

$$H'(\mathbf{q},t) = -e\mathbf{F}(t)\hat{\boldsymbol{\mathcal{A}}}(\mathbf{q},t), \tag{17}$$

$$\hat{\boldsymbol{\mathcal{A}}}(\mathbf{q},t) = \begin{bmatrix} 0 & \boldsymbol{\mathcal{D}}^{cv}(\mathbf{q},t) \\ \boldsymbol{\mathcal{D}}^{vc}(\mathbf{q},t) & 0 \end{bmatrix} \tag{18}$$

where

$$\boldsymbol{\mathcal{D}}^{cv}(\mathbf{q},t) = \boldsymbol{\mathcal{A}}^{cv}[\mathbf{k}(\mathbf{q},t)] \times \exp\left(\mathrm{i}\phi_{cv}^{(\mathrm{D})}(\mathbf{q},t) + \mathrm{i}\phi_{cv}^{(\mathrm{B})}(\mathbf{q},t)\right), \tag{19}$$

$$\phi_{cv}^{(\mathrm{D})}(\mathbf{q},t) = \phi_{v}^{(\mathrm{D})}(\mathbf{q},t) - \phi_{c}^{(\mathrm{D})}(\mathbf{q},t) \tag{20}$$

$$\phi_{cv}^{(\mathrm{B})}(\mathbf{q},t) = \phi_{v}^{(\mathrm{B})}(\mathbf{q},t) - \phi_{c}^{(\mathrm{B})}(\mathbf{q},t) \tag{21}$$

$$\boldsymbol{\mathcal{A}}^{cv}(\mathbf{q}) = \left\langle \Psi_{\mathbf{q}}^{(c)} | \mathrm{i}\frac{\partial}{\partial \mathbf{q}} | \Psi_{\mathbf{q}}^{(v)} \right\rangle. \tag{22}$$

Here $\boldsymbol{\mathcal{A}}^{cv}(\mathbf{q})$ is a matrix element of the non-Abelian Berry connection [40–42], which has the following expression

$$\mathcal{A}_x^{cv}(\mathbf{k}) = \mathcal{N}\left(\frac{-a}{2|f(\mathbf{k})|^2}\right)\left(\sin\frac{ak_x}{2}\sin\frac{a\sqrt{3}k_y}{2} + \mathrm{i}\frac{\Delta_g}{2E_c}\left(\cos\frac{a\sqrt{3}k_y}{2}\sin\frac{ak_x}{2} + \sin ak_x\right)\right) \tag{23}$$

$$\mathcal{A}_y^{cv}(\mathbf{k}) = \mathcal{N}\left(\frac{a}{2\sqrt{3}|f(\mathbf{k})|^2}\right)\left(-1 - \cos\frac{a\sqrt{3}k_y}{2}\cos\frac{ak_x}{2} + 2\cos^2\frac{ak_x}{2} - \mathrm{i}\frac{3\Delta_g}{2}E_c\sin\frac{a\sqrt{3}k_y}{2}\cos\frac{ak_x}{2}\right), \tag{24}$$

where

$$\mathcal{N} = \frac{|\gamma f(\mathbf{k})|}{\sqrt{\frac{\Delta_g^2}{4} + |\gamma f(\mathbf{k})|^2}}.$$

Note that the non-Abelian Berry connection is simply proportional to the interband transition dipole matrix element, $\mathbf{D}(\mathbf{k}) = e\boldsymbol{\mathcal{A}}^{\mathrm{cv}}(\mathbf{k})$.

The ultrafast field drives electric current, $\mathbf{J}(t) = \{J_x(t), J_y(t)\}$. The current has both interband and intraband contributions, $\mathbf{J}(t) = \mathbf{J}^{(\mathrm{intra})}(t) + \mathbf{J}^{(\mathrm{inter})}(t)$. The intraband current is proportional to the group velocity and has the following form

$$\mathbf{J}^{(\mathrm{intra})}(t) = \frac{eg_s}{a^2}\sum_{\alpha=\mathrm{c,v},\mathbf{q}} |\beta_\alpha(\mathbf{q},t)|^2\,\mathbf{v}^{(\alpha)}(\mathbf{k}(\mathbf{q},t)), \tag{25}$$

where $\mathbf{v}_{\mathbf{k}}^{(\alpha)} = \frac{\partial}{\partial \mathbf{k}}E^{(\alpha)}(\mathbf{k})$ is the group velocity (intraband velocity) and $g_s = 2$ is the spin degeneracy. The group velocities can be found from equations (5)–(6)

$$V_x^{\mathrm{c}}(\mathbf{k}) = -V_x^{\mathrm{v}}(\mathbf{k}) = \frac{-a\gamma^2}{\hbar\sqrt{|\gamma f(\mathbf{k})|^2 + \frac{\Delta_g^2}{4}}} \times \sin\frac{ak_x}{2}\left(\cos\frac{\sqrt{3}ak_y}{2} + 2\cos\frac{ak_x}{2}\right) \tag{26}$$

$$V_y^{\mathrm{c}}(\mathbf{k}) = -V_y^{\mathrm{v}}(\mathbf{k}) = \frac{-\sqrt{3}a\gamma^2}{\hbar\sqrt{|\gamma f(\mathbf{k})|^2 + \frac{\Delta_g^2}{4}}} \times \sin\frac{\sqrt{3}ak_y}{2}\cos\frac{ak_x}{2}. \tag{27}$$

The interband current is given by the following expression

$$\mathbf{J}^{(\mathrm{inter})}(t) = \mathrm{i}\frac{eg_s}{\hbar a^2}\sum_{\substack{\mathbf{q} \\ \alpha,\alpha'=\mathrm{v,c} \\ \alpha\neq\alpha'}} \beta_{\alpha'}^*(\mathbf{q},t)\beta_\alpha(\mathbf{q},t) \times \exp\{i\phi_{\alpha'\alpha}^{(\mathrm{D})}(\mathbf{q},t) + \mathrm{i}\phi_{\alpha'\alpha}^{(\mathrm{B})}(\mathbf{q},t)\} \times \left[E_{\alpha'}\left(\mathbf{k}(\mathbf{q},t)\right) - E_\alpha\left(\mathbf{k}(\mathbf{q},t)\right)\right]\boldsymbol{\mathcal{A}}^{(\alpha\alpha')}\left(\mathbf{k}(\mathbf{q},t)\right), \tag{28}$$

where

$$\phi_{\alpha'\alpha}^{(\mathrm{D})}(\mathbf{q},t) = \phi_{\alpha}^{(\mathrm{D})}(\mathbf{q},t) - \phi_{\alpha'}^{(\mathrm{D})}(\mathbf{q},t), \tag{29}$$

$$\phi_{\alpha'\alpha}^{(\mathrm{B})}(\mathbf{q},t) = \phi_{\alpha}^{(\mathrm{B})}(\mathbf{q},t) - \phi_{\alpha'}^{(\mathrm{B})}(\mathbf{q},t). \tag{30}$$

3. Results and discussion

In gapped graphene, sublattices A and B are not equivalent, which results in broken inversion symmetry. Gapped graphene is symmetric with respect to the y-axis, but there is no symmetry with respect to the x-axis, see figure 1. Thus, if the linear optical pulse is polarized along the y-axis, then the CB population distribution in the reciprocal space is symmetric with respect to the y-axis and the electric current is generated only along the y-axis, and not along the x-axis. But if the pulse is polarized along the x-axis, the current is expected to flow both along the x and y directions. Below we consider only this case, i.e. we assume that the optical pulse is polarized along the x-axis.

We consider a linearly x-polarized ultrafast optical pulse that is applied normally on the gapped graphene monolayer and has the following waveform

$$F = F_0(1 - 2u^2)\mathrm{e}^{-u^2}, \tag{31}$$

where F_0 is the amplitude of the pulse, $u = t/\tau$, and $\tau = 1$ fs. We assume that the pulse is polarized along the x-axis. It should be mentioned that the x-axis is not the axis of symmetry of the gapped graphene, while the y-axis is the axis of symmetry.

In the presence of the pulse, we solve the TDSE assuming that the VB is initially occupied and the CB is empty. The electron dynamics in the field of the pulse is highly nonlinear and is characterized by the redistribution of electrons between the VB and CB. After the pulse, there is a nonzero

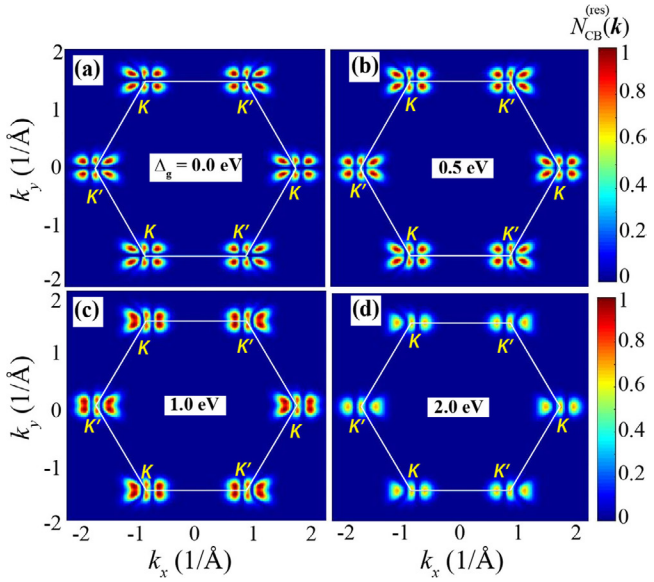

Figure 2. The residual CB population $N_{CB}^{(res)}(\mathbf{k})$ for gapped graphene with various band gaps, $\Delta_g = 0, 0.5, 1$ eV, and $\Delta_g = 2$ eV, in the extended zone picture. The white solid line shows the boundaries of the first Brillouin zone with the K, K'-points indicated. The applied field is a pulse linearly polarized in the x direction, and its amplitude is 0.5 V Å^{-1}.

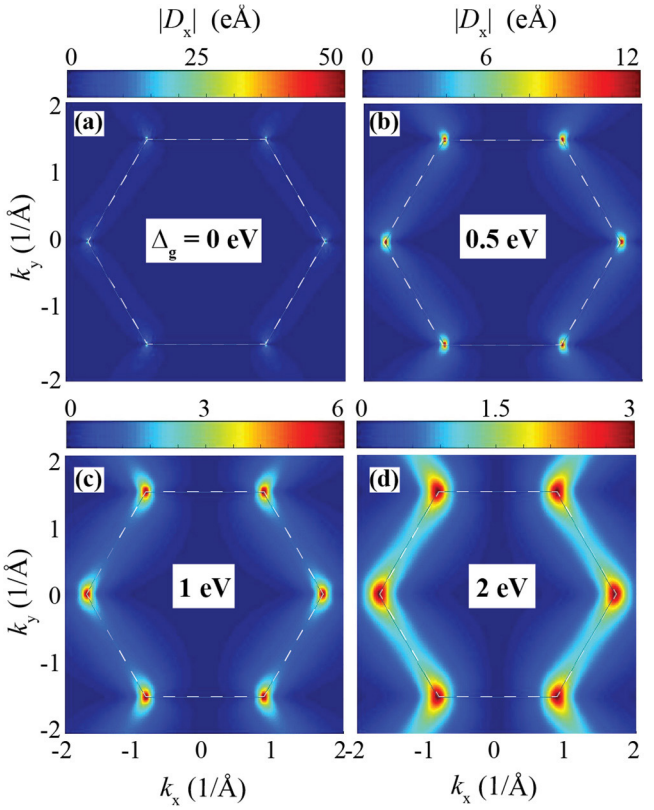

Figure 3. The absolute value of the x component of the dipole matrix element is shown for gapped graphene with various band gaps (a) 0, (b) 0.5 eV, (c) 1.5 eV, and (d) 2 eV. The dash white line shows the boundary of the first Brillouin zone.

residual electron population, $N_{CB}^{(res)}$, in the CB—see figure 2. Such a population determines the irreversibility of the electron dynamics. The distributions of $N_{CB}^{(res)}$ in the reciprocal space are shown in figures 2(a)–(d) for different values of the band gap. The distributions are characterized by hot spots with large, ~ 1, CB population. Such hot spots are due to the double passage of electrons of the K (K') point during the pulse and the manifestation of the interference pattern. Similar hot spots were discussed in [43], where the interaction of a linear optical pulse with pristine graphene has been studied. For gapped graphene, the interference pattern becomes smeared, see figure 2. This is because the interband coupling is determined by the interband transition dipole matrix element, the distribution of which is broadened with increasing the band gap—see figure 3. At the same time, the separation between the fringes is inversely proportional to the nonlocality distance and, thus, does not depend on the band gap [43]. Another interesting property of the CB population distribution is that it is symmetric with respect to both x and y axes. This is a nontrivial property since the x-axis is not the axis of symmetry of the system.

The CB population distribution is shown in figures 4(a)–(d) at different moments of time. It illustrates the formation of the interference-induced hot spots in the CB population distribution. At all moments, the CB population distribution is symmetric with respect to the x axis. Initially, at -2.5 fs $\leqslant t \leqslant -0.7$ fs, the applied field is negative, so the electrons are accelerated to the right. Since the interband coupling is strong near K and K' points only—see figure 3, the CB population within this time interval is large on the left side of the K and K' points, see figure 4 (a).

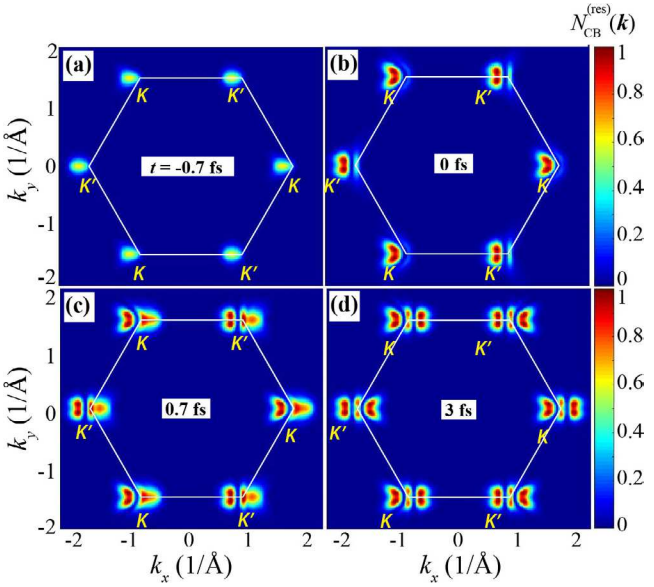

Figure 4. The CB population, $N_{CB}(\mathbf{k})$, as a function of the initial crystal momentum (in the extended zone picture) for gapped graphene with band gap 1 eV for different moments of time, $t = -0.7, 0, 0.7$ fs, and $t = 3$ fs. The white solid line shows the boundaries of the first Brillouin zone with the K, K'-points indicated. The applied pulse is linearly polarized in the x direction, and its amplitude is 0.5 V Å^{-1}.

For the time interval -0.7 fs $\leqslant t \leqslant 0$ fs, the field is positive and the electrons move to the left and pass the K and K'

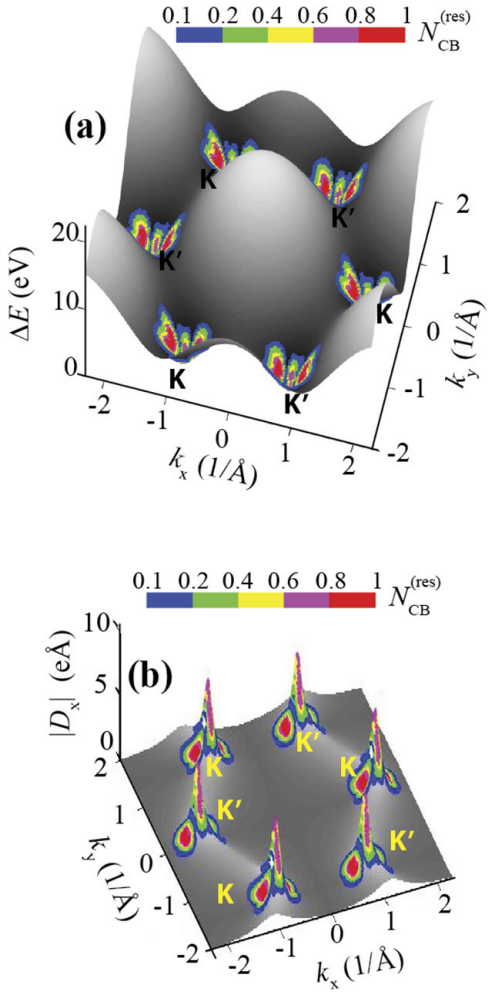

Figure 5. (a) The electron–hole excitation energy $E_c(\mathbf{k}) - E_v(\mathbf{k})$ in the first Brillouin zone shown in the grayscale for gapped graphene with band gap $\Delta_g = 1$ eV. The population of the CB is superimposed on the energy landscape and is color-coded. The applied pulse is linearly polarized in the x direction with the amplitude of 0.5 V Å^{-1}. (b) For the same system, the interband matrix element in the x direction, $|D_x|$ is plotted in the grayscale. The color-coded residual CB population is superimposed.

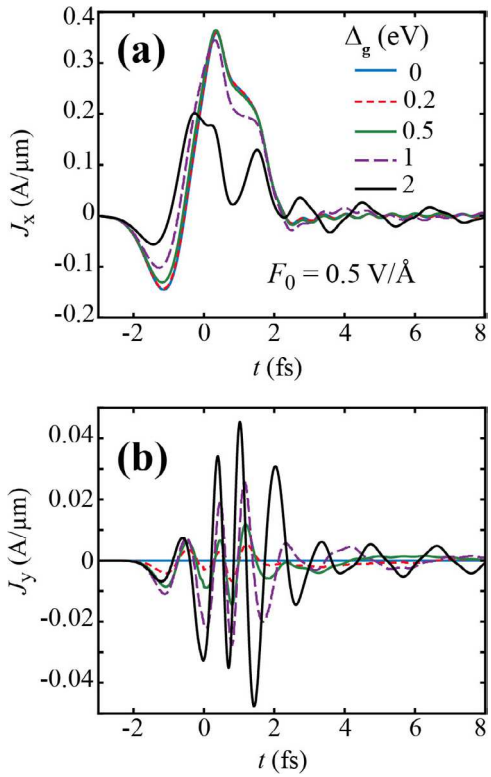

Figure 6. The current densities in gapped graphene are shown as a function of time for various band gaps, 0 eV, 0.2 eV, 0.5 eV, 1 eV, and 2 eV. The applied pulse is linearly polarized in the x-direction, and its amplitude is 0.5 V Å^{-1}. (a) The current density, J_x, is along the direction of the applied field. (b) The current density, J_y, is in the direction normal to the applied field.

points the second time, which results in interference fringes or hot spots on the left sides of the valleys as shown in figure 4(b). The field remains positive for 0 fs $\leqslant t \leqslant$ 0.7 fs and now the electrons from the right side of K and K' points pass the region near K or K' points, which results in large CB population on the right side of the K and K' points, see figure 4(c). The field changes its sign at 0.7 fs $\leqslant t \leqslant$ 2.5 fs. Then the electrons from the right side of K and K' points pass through the region of large interband coupling the second time, which produces hot spots of CB population on the right side of the K and K' points. The electron CB distributions shown in figures 2 and 4 could be observed by time resolve angle-resolved photoelectron spectroscopy (tr-ARPES) [44, 45].

The strong field of the excitation pulse coherently populates electron–hole states in the CB in a very wide band of excitation energies that is determined mostly by the amplitude of the pulse but not by its spectral composition. To illustrate this, in figure 5(a) we plot the CB electron population superimposed on the energy dispersion for the gapped graphene with a band gap of 1 eV. As we can see in this figure, the ultrashort optical pulse with the amplitude of 0.5 V Å^{-1} excites the electron–hole pairs in the energy band as high as $\Delta E \sim 7$ eV. This bandwidth significantly exceeds the spectral width of the 2 fs excitation pulse, which is ~ 2 eV.

The physics of this process can be understood as the following. The optical field compels electrons to move in the reciprocal space, according to Bloch equation (8). During this motion, some electrons pass close to the K-points. At these points, the interband matrix element (non-Abelian Berry curvature) of equation (22) is greatly enhanced—see figure 5(b) and also figure 3. Thus, these electrons have a high probability of undergoing the VB→CB transitions. After the pulse ends, electrons return to their original positions in the Brillouin zone, and their energy distribution reflects the work that the optical field did on them during the pulse. This large spectral bandwidth of the electron–hole excitations also allows one to measure the temporal dynamics of the electron population with a fundamental resolution $\Delta t \sim \hbar/\Delta E \sim 100$ fs limited by the Heisenberg uncertainty relation.

Redistribution of electrons between the VB and CB during the pulse generates an electric current. For the pulse polarized along the x-axis, which is not the axis of symmetry for the gapped graphene, both the longitudinal current, i.e. current in the x direction, and the transverse current, i.e. current in the y direction, are generated. Such currents are shown in figure 6

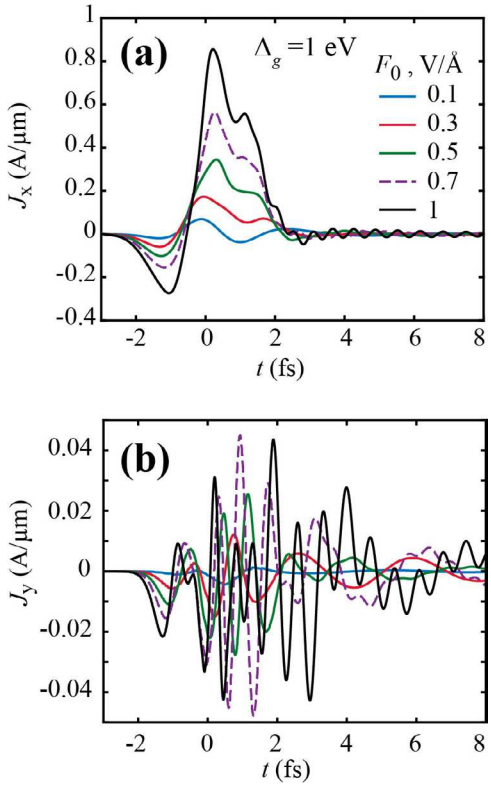

Figure 7. The current densities in gapped graphene are shown as a function of time for various field amplitudes, $F_0 = 0.1, 0.3, 0.5, 0.7, 1.0$ VÅ^{-1}. The applied pulse is linearly polarized in the x-direction, and the band gap of gapped graphene is $\Delta_g = 1$ eV. (a) The current density, J_x, is along the direction of the applied field. (b) The current density, J_y, in the direction normal to the applied field.

for different values of the band gap, Δ_g. For zero band gap, i.e. for pristine graphene, the transverse current, J_y, is zero. The transverse current increases with the band gap.

The electric current, which is generated during the pulse, has two contributions: intraband and interband—see equations (25) and (28). The intraband current (25) is entirely determined by the electron density distributions in the CB and VB. It can, therefore, be considered as a measure of the asymmetry of such distributions. Due to the excitation pulse being invariant with respect to the reflection in the x axis, the CB population distribution is mirror-symmetric with respect to that axis, both during the pulse and after it. Consequently, the intraband transverse current is zero. Thus, the transverse current, J_y, for gapped graphene is determined by the interband contribution only. As the results, the transverse current, J_y, as a function of time, is oscillating with the frequency that depends on the band gap, see figure 6(b). At the same time, the longitudinal current, J_x, is almost unidirectional with some oscillations, see figure 6(a). Note that these oscillations increase with the band gap; for the maximum band gap, $\Delta_g = 2$ eV, the strong oscillations start at the end of the excitation pulse, i.e. at $t \gtrsim 1$ fs. These oscillations are due to the interband component of the current that is superimposed on the non-oscillating intraband component causing a 'beating' pattern that is well pronounced for $t \approx 1$ fs.

Since the band gap determines the strength of the asymmetry of the system, we expect that the magnitude of the transverse current increases with band gap, which is shown in figure 6(b). For the longitudinal current, there is a different tendency. The longitudinal current first increases with Δ_g and then, at large band gaps, $\Delta_g \sim 2$ eV, decreases. Such suppression of the longitudinal current at large values of Δ_g is due to the specific dependence of the interband dipole matrix elements (non-Abelian Berry connection) on the band gap. As shown in figure 3, at small band gaps, the interband dipole matrix element is strongly localized near the K and K' points. With increasing band gap, the dipole matrix element becomes delocalized and nonzero at the large part of the Brillouin zone, where the maximum of the dipole matrix element decreases with band gap keeping the net dipole matrix element, i.e. the integral of the dipole matrix element over the whole Brillouin zone, constant. As a result, the total CB population near the K or K' points decreases with Δ_g, which finally results in suppression of the longitudinal current.

In figure 7, the longitudinal and transverse currents are shown for different field amplitudes. As expected, with increasing field amplitude, the magnitudes of both currents increase. The frequency of oscillations of the transverse current also depends on the magnitude of the pulse, while the longitudinal current is almost unidirectional.

The direction of the current is determined by the direction of the field maximum. For the field profile (31), the field maximum points in the positive direction of the x-axis. If we change the direction of the field maximum to the negative one, i.e. it is pointing in the negative direction of the x-axis, then the longitudinal current, J_x, changes its sign, while the transverse current, J_y, remains the same. The transverse current changes its sign if we change the signs of the on-site energies of sublattices A and B, i.e. change the sign of parameter Δ_g in Hamiltonian (3).

The generated electric current during the pulse results in the transfer of an electric charge through the system. This transferred charge can be calculated as

$$\mathbf{Q} = \int_{-\infty}^{\infty} \mathbf{J}(t)\mathrm{d}t. \tag{32}$$

For the pulse polarized along the x-axis, the charge is transferred in both x and y directions. In figure 8, the transferred charge is shown as a function of the pulse amplitude for different values of the band gap. As expected, for zero band gap, there is no charge transfer in the transverse direction, $Q_y = 0$—see figure 8(a). As a function of the field amplitude, the transverse transferred charge shows oscillations, which is due to oscillations in the transverse current as a function of time. The longitudinal transferred charge, Q_x, monotonically increases with the field amplitude and has a weak dependence on the band gap—see figure 8(b). At large band gap, $\Delta_g \sim 2$ eV, transferred charge Q_x becomes smaller, which is related to the suppression of the CB population and correspondingly the longitudinal electric current at large Δ_g.

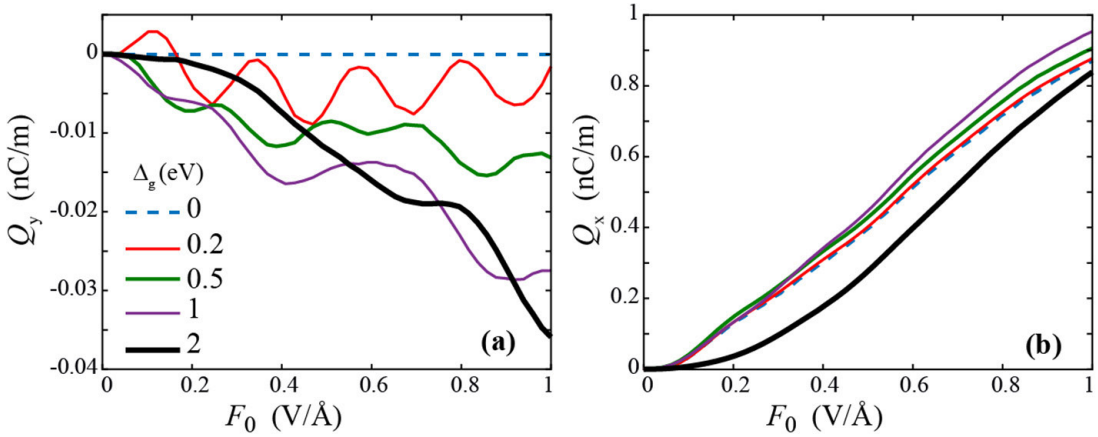

Figure 8. The transferred charge densities are shown as a function of the field amplitude, F_0, for different band gaps, 0 eV (case of graphene), 0.2 eV, 0.5 eV, 1 eV, and 2 eV. (a) The transferred charge density is shown in the direction normal to the applied field, Q_y, and (b) The transferred charge density is shown along the direction of the field, Q_x. The applied pulse is linearly polarized in the x-direction.

4. Conclusion

In pristine graphene, which has inversion symmetry, there are two axes of symmetry, say x and y. If an external linear pulse is polarized along with these two directions, then it will produce CB population distribution that is symmetric with respect to the axis of polarization of the pulse. The pulse will also generate an electric current, and the corresponding transferred charge along the direction of polarization only, but not in the transverse direction.

For gapped graphene, the inversion symmetry is broken. In this case, there is only one axis of symmetry, say the y-axis. If the linear pulse is polarized along the x axis, since this axis is not the axis of symmetry, electric current is generated in both x and y directions. The transverse current does not depends on the direction of the field maximum, while the longitudinal current changes its sign when the direction of the peak is reversed. At the same time, for the same polarization of the pulse, i.e. along the x-axis, similar to pristine graphene, the CB population distribution is symmetric with respect to the x-axis both during and after the pulse. This means that the electron dynamics above ($k_y > 0$) and below ($k_y < 0$) the K (K') point is exactly the same, which results in a symmetric CB population distribution. Although, the electron dynamics depends on the geometric phase, which is different above and below the K (K') point, this phase is exactly canceled by the phase of the interband dipole matrix element (non-Abelian Berry connection). This is a property of the two-band model of gapped graphene, which will be discussed somewhere else. If more bands are included in the model, then there will be no cancellation of the geometric phase and the net (topological) phase, which is the sum of the geometric phase and the phase of the interband dipole coupling will be nonzero. The topological phase has different time dependence above and below the K (K'), which results in topological resonance. This topological resonance occurs due to a partial cancellation of the dynamic phase by the topological phase. Such partial cancellation is different above and below the K (K') point, which finally results in different CB populations and asymmetric CB population distribution. Such small asymmetry of CB population introduces small intraband contributions to the transverse current.

Acknowledgments

Major funding was provided by Grant No. DE-SC0007043 from the Materials Sciences and Engineering Division of the Office of the Basic Energy Sciences, Office of Science, U.S. Department of Energy. Numerical simulations were performed using support by Grant No. DE-FG02-01ER15213 from the Chemical Sciences, Biosciences, and Geosciences Division, Office of Basic Energy Sciences, Office of Science, U.S. Department of Energy. The work of VA was supported by NSF EFRI NewLAW Grant No EFMA-1741691 with the sub-award No. T883032. Support for SAOM came from MURI Grant No. FA9550-15-1-0037 from the U.S. Air Force Office of Scientific Research and Office of Naval Research (DOD)Grant No. N000-14-17-1-2588 with the sub-award No. 24086151.

ORCID iDs

S Azar Oliaei Motlagh https://orcid.org/0000-0002-6732-8946
Fatemeh Nematollahi https://orcid.org/0000-0003-2781-6723
Aranyo Mitra https://orcid.org/0000-0002-6654-9042
Mark I Stockman https://orcid.org/0000-0002-6996-0806

References

[1] Schiffrin A *et al* 2012 Optical-field-induced current in dielectrics *Nature* **493** 70–4
[2] Apalkov V and Stockman M I 2012 Theory of dielectric nanofilms in strong ultrafast optical fields *Phys. Rev.* B **86** 165118
[3] Higuchi T, Heide C, Ullmann K, Weber H B and Hommelhoff P 2017 Light-field-driven currents in graphene *Nature* **550** 224–8

[4] Elisabeth G *et al* 2016 Ultrafast electronic response of graphene to a strong and localized electric field *Nat. Commun.* **7** 13948

[5] Oliaei Motlagh S A, Apalkov V and Stockman M I 2017 Interaction of crystalline topological insulator with an ultrashort laser pulse *Phys. Rev.* B **95** 085438

[6] Motlagh S A O, Wu J S, Apalkov V and Stockman M I 2018 Fundamentally fastest optical processes at the surface of a topological insulator *Phys. Rev.* B **98** 125410

[7] Nematollahi F, Motlagh S A O, Apalkov V and Stockman M I 2019 Weyl semimetals in ultrafast laser fields *Phys. Rev.* B **99** 245409

[8] Heide C, Higuchi T, Weber H B and Hommelhoff P 2018 Coherent electron trajectory control in graphene *Phys. Rev. Lett.* **121** 207401

[9] You Y S, Yin Y, Wu Y, Chew A, Ren X, Zhuang F, Gholam-Mirzaei S, Chini M, Chang Z and Ghimire S 2017 High-harmonic generation in amorphous solids *Nat. Commun.* **8** 724

[10] Liu H Z, Li Y L, You Y S, Ghimire S, Heinz T F and Reis D A 2017 High-harmonic generation from an atomically thin semiconductor *Nat. Phys.* **13** 262–6

[11] Kaiser A, Rethfeld B, Vicanek M and Simon G 2000 Microscopic processes in dielectrics under irradiation by subpicosecond laser pulses *Phys. Rev.* B **61** 11437–50

[12] Heide C, Boolakee T, Higuchi T, Weber H B and Hommelhoff P 2019 Interaction of carrier envelope phase-stable laser pulses with graphene: the transition from the weak-field to the strong-field regime *New J. Phys.* **21** 045003

[13] Sun D, Aivazian G, Jones A M, Ross J S, Yao W, Cobden D and Xu X 2012 Ultrafast hot-carrier-dominated photocurrent in graphene *Nat. Nanotechnol.* **7** 114

[14] Mashiko H, Chisuga Y, Katayama I, Oguri K, Masuda H, Takeda J and Gotoh H 2018 Multi-petahertz electron interference in cr:al2o3 solid-state material *Nat. Commun.* **9** 1468

[15] Shin H J, Nguyen V L, Lim S C and Son J-H 2018 Ultrafast nonlinear travel of hot carriers driven by high-field terahertz pulse *J. Phys. B: At. Mol. Opt. Phys.* **51** 144003

[16] Trushin M lit *et al* 2015 Ultrafast pseudospin dynamics in graphene *Phys. Rev.* B **92** 165429

[17] Kelardeh H K, Apalkov V and Stockman M I 2017 Graphene superlattices in strong circularly polarized fields: chirality, Berry phase, and attosecond dynamics *Phys. Rev.* B **96** 075409

[18] Motlagh Oliaei S A, Wu J-S, Apalkov V and Stockman M I 2018 Femtosecond valley polarization and topological resonances in transition metal dichalcogenides *Phys. Rev.* B **98** 081406

[19] Sun D, Lai J W, Ma J C, Wang Q S and Liu J 2017 Review of ultrafast spectroscopy studies of valley carrier dynamics in two-dimensional semiconducting transition metal dichalcogenides *Chin. Phys.* B **26** 037801

[20] Zhang J, Ouyang H, Zheng X, You J, Chen R, Zhou T, Sui Y, Liu Y, Cheng X and Jiang T 2018 Ultrafast saturable absorption of mos2 nanosheets under different pulse-width excitation conditions *Opt. Lett.* **43** 243–6

[21] Butler S Z *et al* 2013 Progress, challenges, and opportunities in two-dimensional materials beyond graphene *ACS Nano* **7** 2898–926

[22] Geim A K and Novoselov K S 2007 The rise of graphene *Nat. Mater.* **6** 183–91

[23] Neto A H C, Guinea F, Peres N M R, Novoselov K S and Geim A K 2009 The electronic properties of graphene *Rev. Mod. Phys.* **81** 109–62

[24] Novoselov K S, Geim A K, Morozov S V, Jiang D, Katsnelson M I, Grigorieva I V, Dubonos S V and Firsov A A 2005 Two-dimensional gas of massless Dirac fermions in graphene *Nature* **438** 197–200

[25] Kormanyos A, Burkard G, Gmitra M, Fabian J, Zolyomi V, Drummond N D and Fal'ko V 2015 K.p theory for two-dimensional transition metal dichalcogenide semiconductors *2D Mater.* **2** 022001

[26] Jiang J W 2015 Graphene versus MoS_2: a short review *Frontiers Phys.* **10** 287–302

[27] Ye Y, Xiao J, Wang H L, Ye Z L, Zhu H Y, Zhao M, Wang Y, Zhao J H, Yin X B and Zhang X 2016 Electrical generation and control of the valley carriers in a monolayer transition metal dichalcogenide *Nat. Nanotechnol.* **11** 598–602

[28] Jariwala D, Sangwan V K, Lauhon L J, Marks T J and Hersam M C 2014 Emerging device applications for semiconducting two-dimensional transition metal dichalcogenides *ACS Nano* **8** 1102–20

[29] Oliaei Motlagh S A, Nematollahi F, Apalkov V and Stockman M I 2019 Topological resonance and single-optical-cycle valley polarization in gapped graphene *Phys. Rev.* B **100** 115431

[30] Nevius M S, Conrad M, Wang F, Celis A, Nair M N, Taleb-Ibrahimi A, Tejeda A and Conrad E H 2015 *Semiconducting graphene from highly ordered substrate interactions Phys. Rev. Lett.* **115** 136802

[31] Jariwala D, Srivastava A and Ajayan P M 2011 Graphene synthesis and band gap opening *J. Nanosci. Nanotechnol.* **11** 6621–41

[32] Hwang E H and Das Sarma S 2008 Single-particle relaxation time versus transport scattering time in a two-dimensional graphene layer *Phys. Rev.* B **77** 195412

[33] Breusing M, Kuehn S, Winzer T, Malic E, Milde F, Severin N, Rabe J P, Ropers C, Knorr A and Elsaesser T 2011 Ultrafast nonequilibrium carrier dynamics in a single graphene layer *Phys. Rev.* B **83** 153410

[34] Malic E, Winzer T, Bobkin E and Knorr A 2011 Microscopic theory of absorption and ultrafast many-particle kinetics in graphene *Phys. Rev.* B **84** 205406

[35] Brida D *et al* 2013 Ultrafast collinear scattering and carrier multiplication in graphene *Nat. Commun.* **4** 1987

[36] Gierz I, Petersen J C, Mitrano M, Cacho C, Turcu I C, Springate E, Stohr A, Kohler A, Starke U and Cavalleri A 2013 Snapshots of non-equilibrium Dirac carrier distributions in graphene *Nat. Mater.* **12** 1119–24

[37] Tomadin A, Brida D, Cerullo G, Ferrari A C and Polini M 2013 Nonequilibrium dynamics of photoexcited electrons in graphene: collinear scattering, Auger processes, and the impact of screening *Phys. Rev.* B **88** 035430

[38] Pedersen T G, Jauho A-P and Pedersen K 2009 Optical response and excitons in gapped graphene *Phys. Rev.* B **79** 113406

[39] Houston W V 1940 Acceleration of electrons in a crystal lattice *Phys. Rev.* **57** 184–6

[40] Wilczek F and Zee A 1984 Appearance of gauge structure in simple dynamical systems *Phys. Rev. Lett.* **52** 2111–4

[41] Xiao D, Chang M-C and Niu Q 2010 Berry phase effects on electronic properties *Rev. Mod. Phys.* **82** 1959–2007

[42] Yang F and Liu R B 2014 Nonlinear optical response induced by non-Abelian Berry curvature in time-reversal-invariant insulators *Phys. Rev.* B **90** 245205

[43] Kelardeh H K, Apalkov V and Stockman M I 2015 Graphene in ultrafast and superstrong laser fields *Phys. Rev.* B **91** 045439

[44] Liu Y, Bian G, Miller T and Chiang T C 2011 Visualizing electronic chirality and Berry phases in graphene systems using photoemission with circularly polarized light *Phys. Rev. Lett.* **107** 166803

[45] Kemper A F, Sentef M A, Moritz B, Devereaux T P and Freericks J K 2017 Review of the theoretical description of time-resolved angle-resolved photoemission spectroscopy in electron-phonon mediated superconductors *Ann. Phys., Berlin* **529** 1600235